JGR Atmospheres

RESEARCH ARTICLE
10.1029/2020JD033629

The Peculiar Trajectory of Global Warming

S. Fueglistaler[1,2] **and L.G. Silvers**[2,3]

[1]Department of Geosciences, Princeton University, Princeton, NJ, USA, [2]Program in Atmospheric and Oceanic Sciences, Princeton University, Princeton, NJ, USA, [3]School of Marine and Atmospheric Sciences, State University of New York at Stony Brook, Stony Brook, NY, USA

Key Points:

- Difference between sea surface temperatures (SSTs) in regions of tropical deep convection and average (Δ^{conv}) explains time-varying cloud radiative feedback ("pattern effect")
- SST reconstructions show an unprecedented trend in Δ^{conv} in the 1980s–1990s not seen in coupled atmosphere-ocean general circulation models (GCMs)
- Independent confirmation of the resulting negative cloud feedback in the 1980s–1990s in GCM simulations with observed SSTs is lacking

Correspondence to:
S. Fueglistaler,
stf@princeton.edu

Citation:
Fueglistaler, S., & Silvers, L.G. (2021). The peculiar trajectory of global warming. *Journal of Geophysical Research: Atmospheres*, *126*, e2020JD033629. https://doi.org/10.1029/2020JD033629

Received 31 JUL 2020
Accepted 5 JAN 2021

Author Contributions:
Conceptualization: S. Fueglistaler
Data curation: S. Fueglistaler
Formal analysis: S. Fueglistaler
Investigation: S. Fueglistaler, L.G. Silvers
Methodology: S. Fueglistaler
Project Administration: S. Fueglistaler
Resources: S. Fueglistaler, L.G. Silvers
Software: S. Fueglistaler
Supervision: S. Fueglistaler
Validation: S. Fueglistaler
Writing – original draft: S. Fueglistaler
Writing – review & editing: S. Fueglistaler, L.G. Silvers

Abstract General Circulation Model (GCM) simulations with prescribed observed sea surface temperature (SST) over the historical period show systematic global shortwave cloud radiative effect (SWCRE) variations uncorrelated with global surface temperature (known as "pattern effect"). Here, we show that a single parameter that quantifies the difference in SSTs between regions of tropical deep convection and the tropical or global average (Δ^{conv}) captures the time-varying "pattern effect" in the simulations using the PCMDI/AMIPII SST recommended for CMIP6. In particular, a large positive trend in the 1980s–1990s in Δ^{conv} explains the change of sign to a strongly negative SWCRE feedback since the late 1970s. In these decades, the regions of deep convection warm about +50% more than the tropical average. Such an amplification is rarely observed in forced coupled atmosphere-ocean GCM simulations, where the amplified warming is typically about +10%. During the post 2000 global warming hiatus Δ^{conv} shows little change, and the more recent period of resumed global warming is too short to robustly detect trends. In the prescribed SST simulations, Δ^{conv} is forced by the SST difference between warmer and colder regions. An index thereof ($SST^{\#}$) evaluated for six SST reconstructions shows similar trends for the satellite era, but the difference between the pre- and the satellite era is substantially larger in the PCMDI/AMIPII SSTs than in the other reconstructions. Quantification of the cloud feedback depends critically on small changes in the shape of the SST probability density distribution. These sensitivities underscore how essential highly accurate, persistent, and stable global climate records are to determine the cloud feedback.

1. Introduction

The large range in equilibrium climate sensitivity (the global average temperature change following a doubling of atmospheric CO_2) of 1.5°–4.5° reported in IPCC AR5 (IPCC, 2013) persists and is even wider (but see also assessment by Sherwood et al. (2020)) in the most recent Coupled Model Intercomparison Project, Phase 6 (CMIP6) simulations (Zelinka et al., 2020). This introduces uncertainty regarding the urgency of introducing measures to curb CO_2 emissions to limit global warming to specified targets, such as a global temperature increase relative to preindustrial times of no more than +1.5°C or +2°C (IPCC, 2018).

The period since the late 1970s is arguably the best suited to provide observational constraints on the sensitivity of present climate due to both the availability of truly global observations provided by satellites, and to less uncertainty in atmospheric aerosol than in earlier decades (Anderson et al., 2003; Jimenez-de-la Cuesta & Mauritsen, 2019; Kiehl, 2007). However, it has been recognized that the cloud radiative feedback may have evolved unexpectedly, providing a strong negative feedback in particular over this best-observed period (Andrews et al., 2018; Ceppi & Gregory, 2017; Gregory et al., 2019; Silvers et al., 2018; Zhou et al., 2016). At the heart of this so-called "pattern effect" (Stevens et al., 2016) is amplified warming in the regions of tropical deep convection relative to the average surface temperature (Andrews & Webb, 2018; Dong et al., 2019; Fueglistaler, 2019; Miller, 1997; Zhou et al., 2016).

Much of the "pattern effect" in general circulation model (GCM) simulations forced with observed SSTs and in observations can be captured by a parameter that reflects the difference in sea surface temperature (SST) between regions of deep convection and the tropical average. This parameter accounts for the presence of a second mode (the first being average SST) that induces changes in the static stability of the tropical atmosphere. Zhou et al. (2016) show that the difference in tropical SSTs in regions of strong ascent (determined by the model's midtropospheric vertical winds) and the tropical mean explains changes in stratification which in turn affect in particular the low cloud cover. Similarly, Dong et al. (2019) find that the warming

over the tropical Western Pacific (where most deep convection resides) relative to the average is key to the pattern effect. The formulation of the parameter used here follows the work of Flannaghan et al. (2014) and Fueglistaler (2019), and is deliberately oblivious to the geographic pattern of SSTs as the specific geographic location of deep convection is secondary to this problem. The approach is on safe theoretical grounds in the tropics (see also Y. Zhang & Fueglistaler, 2020) and observations of tropical SSTs, atmospheric temperature and top-of-atmosphere radiative fluxes are consistent with expectations (Fueglistaler, 2019). The fact that also extratropical cloud cover is correlated with an index characterizing the tropical state should not surprise in light of well-established teleconnections (see also Dong et al., 2019; Hoskins & Karoly, 1981; Horel & Wallace, 1981; O'Reilly et al., 2019; Po-Chedley et al., 2018; Trenberth et al., 1998), but the connection lacks the solid theoretical basis of that in the tropics.

We use two metrics to estimate the difference between the conditions in the regions of deep convection and the tropical average: (i) Δ^{conv}, defined as the difference between SSTs in regions of deep convection and the tropical average; and (ii) $SST^{\#}$, defined as the warmest 30% minus the tropical average SST (Fueglistaler, 2019). $SST^{\#}$ has the advantage that it is defined entirely in terms of SSTs and does not require additional information. It implicitly builds on the fact that tropical deep convection preferentially occurs at the high end of the SST distribution (C. Zhang, 1993; Waliser & Graham, 1993). As such, $SST^{\#}$ may be seen in AMIP simulations with prescribed SSTs as the forcer of Δ^{conv}.

In the following, Section 2.1 demonstrates the correlation between $SST^{\#}$ and Δ^{conv}, and the correlation of these parameters to the cloud field and shortwave cloud radiative effect (SWCRE) feedback. Having established the significance of $SST^{\#}$ and Δ^{conv}, Section 2.2 discusses the evolution of these parameters over the historical period (1870s to present), and differences between six different SST reconstructions. Section 2.3 compares the trends over the satellite period between observational reconstructions and coupled atmosphere-ocean GCMs. Finally, Section 3 discusses the implications of the results also in the context of the ocean-atmosphere dynamics related to the "hiatus" in global warming in the early 2000s.

The results taken at face value suggest that the observational period, in particular the satellite period with the highest quality observations, is peculiar compared to coupled atmosphere-ocean GCM simulations. However, the significant differences in the evolution of $SST^{\#}$ and Δ^{conv} between different observational SST reconstructions highlighted in this work need to be resolved before definitive conclusions regarding the cloud radiative feedback over the observational period are possible.

2. Results

2.1. The Evolution of SWCRE and Low Cloud Concentration in AMIP piForcing Simulations

Atmospheric GCM simulations forced with SSTs based on observations but all other forcings fixed (AMIP-piForcing experiments) show decadal variations (Andrews et al., 2018; Gregory & Andrews, 2016; Silvers et al., 2018; Zhou et al., 2016) in shortwave cloud radiative effect (SWCRE; defined as the outgoing shortwave radiation at the top of the atmosphere under clear sky conditions minus the outgoing shortwave radiation including the reflection from clouds). The variations since the 1870s are dominated by a marked increase in reflected sunlight by clouds since the 1970s (i.e., the SWCRE becomes more negative). Similarly, global average surface temperatures increase substantially since the 1970s. Consequently, clouds appear to be a strong negative feedback to warming since the 1970s, in stark contrast to results from coupled atmosphere-ocean GCM simulations (Zhou et al., 2016). This result has been reproduced with different climate models (Andrews et al., 2018; Dong et al., 2019; Gregory et al., 2019; Silvers et al., 2018), and is summarized in Figure 1 using the results obtained with the AM-4.0 (henceforth AM4) GCM (Zhao et al., 2018a, 2018b) developed by the geophysical fluid dynamics laboratory (GFDL), forced with the PCMDI SST reconstructions (Hurrell et al., 2008) recommended for CMIP6 (henceforth labeled PCMDI/AMIPII, or PCMDI for brevity). While the SWCRE as function of global surface temperature up to the 1970s shows some variations on decadal timescale (Figure 1a), the overall tendency is a decrease with warming (a positive feedback of order 0.5 $W\,m^{-2}\,K^{-1}$ when normalized by global average surface temperature change). This changes in the 1970s, when the SWCRE feedback changes sign and becomes strongly negative (order−0.5 $W\,m^{-2}\,K^{-1}$). Figure 1b shows the implications of the change in the SWCRE feedback for the present. If one would

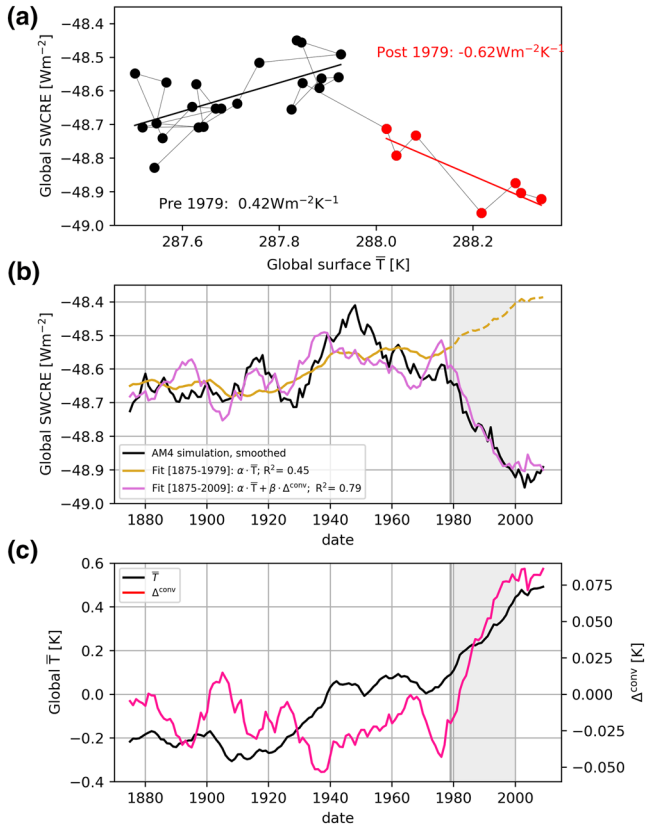

Figure 1. (a) Global average SWCRE as function of global average surface temperature determined from GFDL AM4 model runs (5 ensemble member average) forced with prescribed SSTs (PCMDI/AMIPII), and all other forcings held constant (AMIP-piForcing experiment, data as in Silvers et al. (2018)). Each datapoint is the average over consecutive 5-year periods; the slopes are calculated with a linear regression through the 5-years averages over the periods pre/post1979. (b) Timeseries of global average SWCRE (as in panel a), and the fits from a linear regression against global average surface temperature (goldenrod; $\alpha = 0.37$ W m^{-2} K^{-1} for period 1875–1979; dashed line: extrapolation to 2009), and a multiple linear regression against global average surface temperature and Δ^{conv} (orchid; $\alpha = 0.13$ W m^{-2} K^{-1}; $\beta = -3.44$ W m^{-2} K^{-1}). (c) Timeseries of the explanatory variables global average surface temperature (black, left y-axis) and Δ^{conv} (purple, right y-axis). Data in panels (b) and (c) filtered with 11-years running mean, with first and last 5 years truncated. The start of the satellite era (1979) and the 1980s/1990s period when Δ^{conv} and SWCRE show largest trends are highlighted (gray line, gray shading).

assume that on centennial timescale SWCRE and global average surface temperature are linearly related and extrapolates the linear regression over the period 1875–1979 to the following decades (goldenrod, dashed line), one would underestimate the global SWCRE in 2009 in the model simulations by about 0.5 W m^{-2} (compare the dashed goldenrod line and black line in Figure 1b).

The lack of a strict functional relation between global average SWCRE and average surface temperature evident in Figure 1a challenges the concept of climate sensitivity in terms of global average quantities. The importance of the geographic structure of surface temperature trends led to the term "pattern effect" (Stevens et al., 2016), though in particular in the tropics atmospheric dynamics suggests that to first approximation the problem can be reduced to just one parameter (rather than a large number of distinct patterns). In the tropics, deep convection connects the subcloud layer and the free troposphere such that the free tropospheric temperature is set by the SSTs (more precisely subcloud moist static energy, which also allows to evaluate the problem over land; Y. Zhang & Fueglistaler, 2020) in the regions of deep convection. Conversely, the boundary layer temperature is tied locally to the underlying SSTs and consequently the tropical average boundary layer temperature is a function of tropical average SST. It follows, and is observationally confirmed (Fueglistaler, 2019), that the average boundary layer inversion strength (the difference between free troposphere and boundary layer potential temperature) is proportional to parameters such as Δ^{conv} and SST$^{\#}$ that reflect the difference in SSTs (or subcloud moist static energy) between the convective regions and the average. The boundary layer inversion strength, in turn, affects low cloud amount, with a stronger inversion leading to more clouds (Bretherton, 2015; Klein & Hartmann, 1993; Wood, 2012; Wood & Bretherton, 2006). Observations confirm that the tropical average SWCRE (as reported by CERES/EBAFv4 data; Loeb et al., 2018) is indeed to good approximation a function of tropical average SST and SST$^{\#}$ (Fueglistaler, 2019).

We use precipitation as the weighting function to identify the regions of tropical deep convection (Flannaghan et al., 2014) and define Δ^{conv} as the difference between the precipitation weighted SST, and the tropical average SST ($\overline{SST}$):

$$\Delta^{conv} \equiv \int T \cdot p(T) dT - \overline{T} \quad (1)$$

where T is the monthly mean SST (restricted to tropical ocean; SST substituted by T for better readability), and p is the monthly mean precipitation density (normalized by total precipitation over the tropical oceans) as a function of sea surface temperature. Note that the definition of Δ^{conv} used here is motivated by practical considerations. Mid-tropospheric vertical winds (Bony & Dufresne, 2005; Zhou et al., 2016) hold similar information but rainfall is better observed, and subcloud layer humidity needed for the calculation of moist static energy is not measured globally. As such, Δ^{conv} as defined here should be seen as a reasonable proxy for the difference in subcloud moist static energy between regions of deep convection and the tropical average.

Figure 1b shows that Δ^{conv} and average SST indeed also recover the global average SWCRE variations in the AMIP-piForcing simulations over the historical record. In particular, the multiple linear regression captures the dramatic change in SWCRE in the late 1970s (Figure 1b), attributed to the strong increase in Δ^{conv} from the late 1970s to the late 1990s (Figure 1c). Note that an increase in average SST implies a decrease in cloudiness, while an increase in Δ^{conv} implies an increase in cloudiness. The evolution of the SWCRE as shown

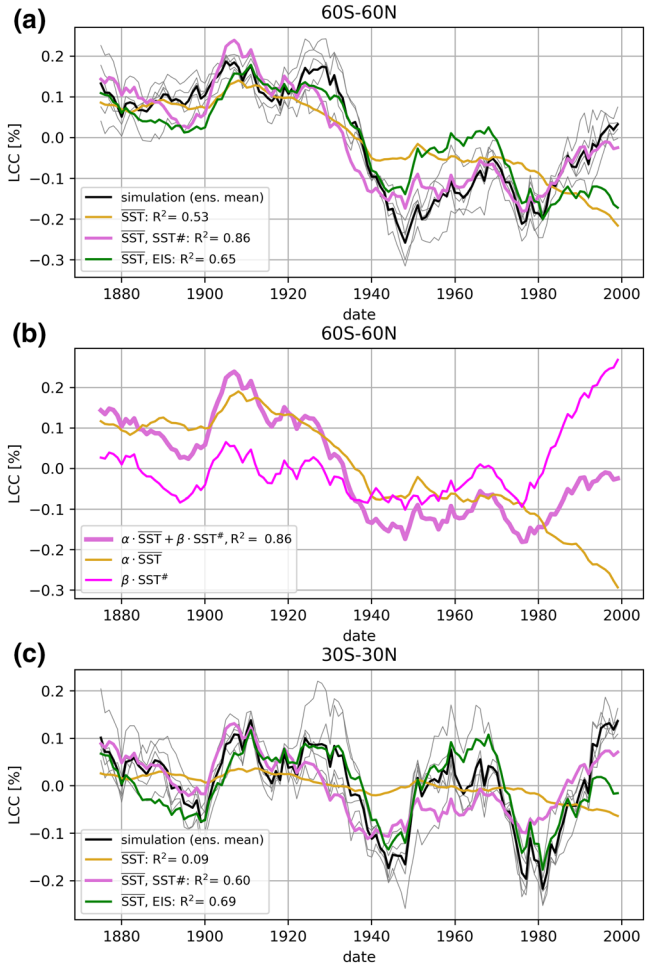

Figure 2. (a) Low Cloud Cover (LCC, in percent) anomalies between 60°S and 60°N in the GFDL AM4 AMIP-piForcing simulations (gray, 5 ensemble members; black line ensemble mean), and results of a linear regression against average SST (goldenrod, $R^2 = 0.53$), and multiple linear regressions against average SST and $SST^{\#}$ (purple, $R^2 = 0.86$), or Estimated Inversion Strength (EIS, green, $R^2 = 0.65$). All annual mean data smoothed with a running-mean over 11 years as in Silvers et al. (2018). (b) The fit of LCC obtained with the multiple linear regression against $\overline{SST}$ and $SST^{\#}$ (purple, identical to purple line in panel (a), and the contributions from the two explanatory variables ($\overline{SST}$: goldenrod (note that the regression slope α is different from that obtained by regression against $\overline{SST}$ only as shown in panel a); $SST^{\#}$: thin magenta). (c) As panel (a), but restricted to the tropics (30°S–30°N).

in Figure 1b from the 1970s onwards is thus the result of two opposing trends, whereby the contribution from the positive trend in Δ^{conv} (SWCRE becomes more negative) is stronger than the contribution from the positive trend in $\overline{SST}$ (SWCRE becomes more positive).

Figure 2a confirms that the SWCRE variations evident in Figure 1 are associated with changes in the Low Cloud Cover (LCC; primarily between 60°S and 60°N) in the GFDL AM4 simulations, and that using $SST^{\#}$ instead of Δ^{conv} yields similar results. Figure 2b shows, similar to Figure 1c, that the multiple linear regression attributes the strong increase in LCC since the 1970s to $SST^{\#}$. While not directly affecting the arguments following in Sections 2.2, these regressions show aspects that reveal uncertainty on the process level that deserve attention in future work: (i) The multiple linear regression of LCC against $\overline{SST}$ and $SST^{\#}$ yields a substantially higher correlation coefficient ($R^2 = 0.86$) than against $\overline{SST}$ and Estimated Inversion Strength (EIS, Wood & Bretherton, 2006; with $R^2 = 0.65$) despite EIS being the more direct physically relevant parameter (in AMIP simulations, $SST^{\#}$ forces Δ^{conv} which in turn affects EIS; but the low clouds are thought to be sensitive to EIS; Klein & Hartmann, 1993; Wood & Bretherton, 2006). (ii) The multiple linear regression applied to only tropical (30°S–30°N) LCC (Figure 2c) yields a similar correlation coefficient when using EIS, but a lower correlation coefficient when using $SST^{\#}$. The weaker correlation obtained when considering the tropics only may in part be related to latitudinal shifts of the cloud fields around 30°S and 30°N, highlighting that the thermodynamic rationale underlying the parameters $SST^{\#}$ and Δ^{conv} may be the primary forcer in the system, but that in limited domains additional factors may play a role. (iii) The two parameters Δ^{conv} and $SST^{\#}$ are correlated (further discussed in Section 2.2) and recover the same overall behavior of Low Cloud Cover over the period 1870–2015. However, in particular on shorter timescales Δ^{conv} and $SST^{\#}$ can diverge, which precludes precise identification of periods of particular interest (i.e., large changes in Δ^{conv} or $SST^{\#}$ over short periods), and whether they may be affected by drifts and discontinuities arising from changes in the observation system.

2.2. Differences in Observational SST Reconstructions, and Similarity of Δ^{conv} and $SST^{\#}$

Figure 3a shows the tropical mean SST evolution since 1870 as represented in six observational reconstructions. Compared to the PCMDI/AMIPII SSTs recommended for CMIP6 and used for the AMIP piForcing simulations discussed above (Figures 1 and 2), in particular the NOAA ERSSTv4 and ERSSTv5 (Huang et al., 2017) stand out with lower temperatures in the first half of the 20th century. Over the satellite era, trend differences in tropical mean SSTs are smaller but the COBE and COBE2 SSTs warm substantially more than the other SSTs (see also Figure 5).

Figure 3b shows the evolution of $SST^{\#}$ calculated for each of the six SST reconstructions. Over the satellite period as a whole, results are similar: during the 1980s and 1990s both $\overline{SST}$ and $SST^{\#}$ show a strong increase, and with the flattening of warming in the late 1990s/early 2000s, $SST^{\#}$ is also approximately constant. In recent years (after about 2010), $\overline{SST}$ is increasing again, but the period is too short to determine whether $SST^{\#}$ follows suit, or not (as visual inspection of Figure 3b suggests). The figure shows substantial differences in the evolution of $SST^{\#}$ between the PCMDI/AMIPII and the HadISST1 SSTs provided by the Hadley Center (Rayner et al., 2003) in the early 1980s when the PCMDI/AMIPII SSTs spin off from the HadISST1 SSTs

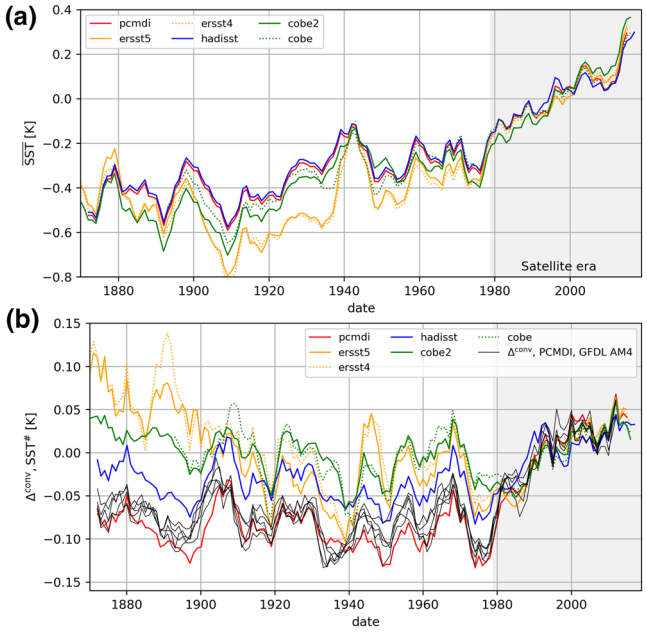

Figure 3. (a) Anomalies of tropical mean SSTs for six different SST reconstructions (PCMDI/AMIPII, ERSSTv5, ERSSTv4, HadISST1, COBE2, COBE; colors as labeled). (b) Anomalies in $SST^{\#}$ determined for the same SST reconstructions (colors, as labeled), and anomalies in Δ^{conv} (black) determined from five ensemble members of GFDL AM4 AMIP-piForcing simulations forced with PCMDI/AMIPII SSTs. Data smoothed with a 5-years running-mean filter for visual clarity; offset calibrated to the period 1979–2014.

(up to the satellite period PCMDI/AMIPII builds on HadISST1, but uses a different method for the satellite era; see Hurrell et al., 2008, Rayner et al., 2003 and discussion in Flannaghan et al., 2014). These differences have a small impact on the linear trend estimates for the period since 1979 (Section 2.3), but have a substantial impact on the difference in $SST^{\#}$ before 1979 relative to the post-1979 period. Taking the correlation of the cloud field with $SST^{\#}$ as seen in the AMIP-piForcing simulations with the PCMDI/AMIPII SSTs discussed above, one would expect a smaller negative cloud feedback since the 1970s in AMIP-piForcing simulations with HadISST1 SSTs. The same is true for the two COBE and the two ERSST SST reconstructions.

In the following, we focus on the satellite period where SSTs are better constrained by observations and rely less on spatio-temporal interpolation which may distort a parameter like $SST^{\#}$ more than $\overline{SST}$ (note that changes in $SST^{\#}$ are about an order of magnitude smaller than changes in $\overline{SST}$, while their impact on the cloud field in Figures 1 and 2 is of comparable magnitude). Moreover, we take advantage of the availability of global precipitation data since 1979, which allows for Δ^{conv} to be calculated from observations. Figure 3(b) shows that in the AMIP piForcing simulations (black lines) the precipitation evolution over the SST field is not strictly tied to $SST^{\#}$ (which explains different atmospheric temperature trends among ensemble members forced with identical SSTs; Fueglistaler et al., 2015), but that over the full timeseries, as well as over the satellite period as a whole, $SST^{\#}$ and Δ^{conv} are highly correlated.

2.3. Coupled Atmosphere-Ocean General Circulation Model Results

Figures 4 and 5 show that the evolution of Δ^{conv} over the satellite period is exceptional compared to trends found in coupled atmosphere-ocean GCM simulations.

Figure 4a shows the evolution of global average SSTs from 1870 to 2075 based on observational reconstructions (up to the present) and model predictions from coupled atmosphere-ocean GCMs. For visual clarity, we show for the observational reconstructions only HadISST1 (blue), PCMDI/AMIPII (red) and NOAA ERSSTv5 (orange). In addition to the observational estimates, the figure shows the CMIP6 (pink, one ensemble per model) and CMIP5 historical simulations (gray, one ensemble per model; see Appendix D), with the CMIP5 historical simulations extended with the Representative Concentration Pathway 8.5 (RCP8.5, a valid approximation to the observed forcing from 2005 to present; Santer et al., 2017) into the future (models listed in Appendix D).

Figure 4b shows the corresponding evolution of Δ^{conv}, additionally showing currently available CMIP6 results for the historical period (up to 2015; pink). Also shown is the evolution of Δ^{conv} in the AMIP-piForcing simulations with GFDL's AM4 using PCMDI/AMIPII SSTs (black, five ensemble members, same runs as shown in Figures 1–3). The observational estimates require observations of precipitation in addition to SSTs. We find that results differ somewhat depending on rainfall data used, and show here the results obtained using rainfall from GPCPv2 (dashed; Adler et al., 2003; Huffman et al., 2001, and CMAP, solid; Xie & Arkin, 1997).

The global average SST evolution from observations and models (Figure 4a) shows reasonable agreement, with well-documented differences. In particular the prominent "hiatus" of warming in the observations over roughly a decade from the early 2000s to the early 2010s (Meehl et al., 2011) is not present in the coupled atmosphere-ocean GCM simulations. Focusing on Δ^{conv}, Figure 4b (see also Figure 3b) shows that during the warming hiatus Δ^{conv} also shows little trend, but that there is a clear difference before and after the late 1970s. In particular, the large positive trend in Δ^{conv} in the 1980s and 1990s has no equivalent in the

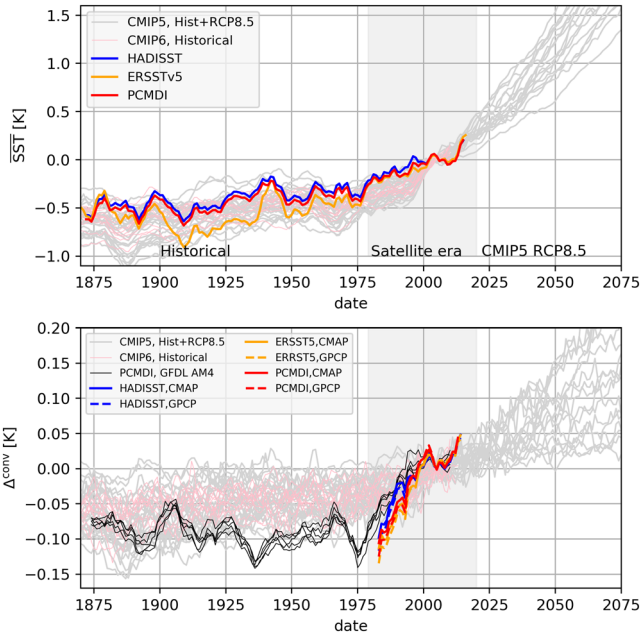

Figure 4. (a) Timeseries of tropical average SST ($\overline{\text{SST}}$) from CMIP5 "historical" (up to year 2005) and 'RCP8.5' coupled GCM simulations (gray), and observational reconstructions (colors, as labeled). (b) Timeseries of Δ^{conv} from CMIP5 "Historical" (up to year 2005) and "RCP8.5" coupled GCM simulations (gray), and CMIP6 "Historical" simulations (pink, up to year 2014), and observational estimates (colors) using SST and rainfall data as labeled. Also shown are five ensembles from the GFDL AM4 AMIP-piForcing simulation using the PCMDI/AMIPII SST. All CMIP model data in both panels shows one ensemble member for each model; all data calibrated to the average of the period 2000–2010, and subsequently smoothed with a 9-years running mean for visual clarity.

coupled GCM simulations (gray, pink) over the historical period prior to the 1970s. However, some of the coupled CMIP5 RCP8.5 GCM simulations show a comparable trend over the 21st century.

Figure 5 shows the trends of the tropical average SST ($\overline{\text{SST}}$, x-axis) and Δ^{conv} (y-axis) over all 36 year periods in the CMIP5 (2,700 segments, light blue) and CMIP6 (2,637 segments, teal) historical simulations (results for the period 1979–2014 with 1-sigma statistical uncertainty indicated), and for the CMIP5 RCP8.5 simulations (1,044 segments; one ensemble member for each model in each scenarios). The figure shows that the large trends in Δ^{conv} in the RCP8.5 simulations with coupled GCMs noted in Figure 4 are associated with large trends in $\overline{\text{SST}}$. That is, a simulation with a strong mean warming (i.e., in $\overline{\text{SST}}$) also shows a large trend in Δ^{conv}. However, the ratio of the two trends is similar across models and the trend in Δ^{conv} is typically about 10% of the trend in $\overline{\text{SST}}$. By contrast, the observations over the period 1979–2015 indicate a strongly amplified temperature trend in regions of deep convection, with the trend in Δ^{conv} about 50% (and higher) of the trend in $\overline{\text{SST}}$. During periods of small trends in $\overline{\text{SST}}$, the ratio of the trends in Δ^{conv} to $\overline{\text{SST}}$ can be very large also in the coupled GCM simulations. However, barely any coupled GCM simulation shows the combination of a large trend in $\overline{\text{SST}}$ and an amplification in the regions of deep convection as large (order 50%) as seen in the observations.

Given that the trend in Δ^{conv} since 1979 arises primarily before the year 2000, we also evaluate trends over 21-year periods (with observational estimate taken for 1979–2000) rather than 36-year periods (see Appendix B). Compared to the period 1979–2015, the amplification ratio in the observations increases (as expected), and the shorter time period leads to a larger statistical uncertainty. Similarly, the coupled atmosphere-ocean GCM simulations yield a larger scatter in trends in Δ^{conv} and $\overline{\text{SST}}$, but also over the shorter period only a handful out of thousands of realizations yield a comparable amplification in the trend of Δ^{conv} at a comparable trend in $\overline{\text{SST}}$.

The trend in Δ^{conv} in the AM4 AMIP-piForcing simulation (Figure 5, black) is smaller than the observational estimates with the same (PCMDI/AMIPII) SST (Figure 5, red; see also Figure 4b, red vs. black lines). Calculation of Δ^{conv} with the rainfall from CMIP6 AMIP (i.e., with all forcing) simulations shows good agreement with the AM4 AMIP-piForcing results (see Appendix A). Thus, while different models and ensembles members yield slightly different Δ^{conv} timeseries, there is a robust difference in Δ^{conv} due to differences in precipitation between the AMIP and AMIP-piForcing simulations on the one hand, and the observations (GPCP and CMAP) on the other hand. These differences indicate subtle but systematic differences in the evolution of the relation between the geographic pattern in SSTs and rainfall as reported by GPCP and CMAP on the one hand, and GCMs run with prescribed SSTs on the other hand.

Figure 6 shows the details (annual means, and 3-years running means instead of 9-years running means as in Figure 4) of the evolution of Δ^{conv} (data as in Figure 4) over the period 1970–2019. Close inspection of the timeseries suggests that the introduction of Special Sensor Microwave/Imager (SSM/I) precipitation estimates following its launch in July 1987 (Adler et al., 2003; Allan et al., 2010; Smith et al., 2009) may have led to a spurious shift in the geographic rainfall pattern that contributes to the discrepancy before about 1988 (compare AM4 AMIP-piForcing experiment in black, with red and blue lines showing the observational estimates). However, prominent differences between observations and the AMIP simulation persist throughout the 1980s and 1990s, and it is these differences that lead to the smaller trend in Δ^{conv} in the AM4 AMIP-piForcing simulations compared to the observational estimates as shown in Figure 5. These differences imply uncertainty in the trend of Δ^{conv} due to uncertainty in rainfall that deserve attention

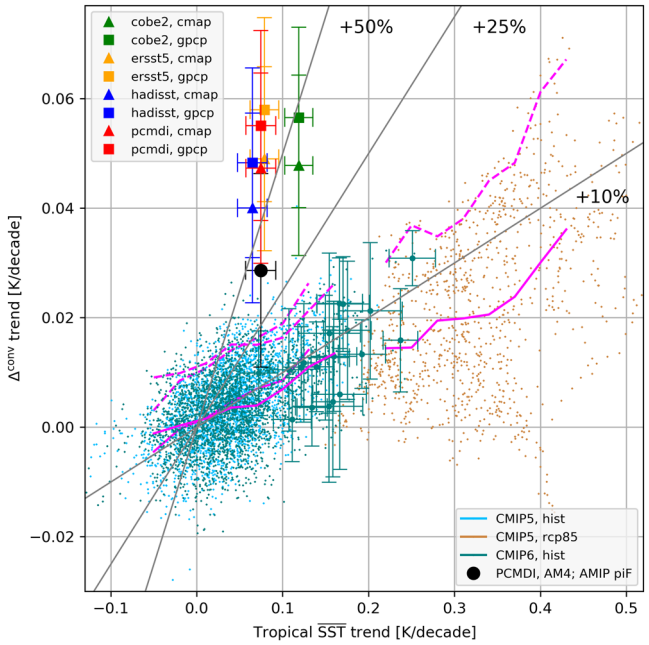

Figure 5. Scatter plot of trends in tropical average SST ($\overline{SST}$, *x*-axis) against trends in Δ^{conv} (*y*-axis), evaluated over 36-year periods. Colors and symbols as labeled; one ensemble per model over all (including overlapping) 36-year periods. Shown in magenta are the average (solid) and 95-percentile (dashed) Δ^{conv} trends as function of trend in $\overline{SST}$ for each experiment (CMIP5 and CMIP6 historical, CMIP5 RCP8.5). Average and 95-percentile calculated only for $\overline{SST}$ trend bins with more than 50 data points. The observational estimates (as labeled in legend) and the CMIP6 model trends of the specific period 1979–2014 are shown with their 1-sigma statistical error. Gray lines indicate where the trend in Δ^{conv} is 10%, 25%, and 50% of the trend $\overline{SST}$ (i.e., SST trends in regions of deep convection are larger by that percentage than the tropical average SST trend).

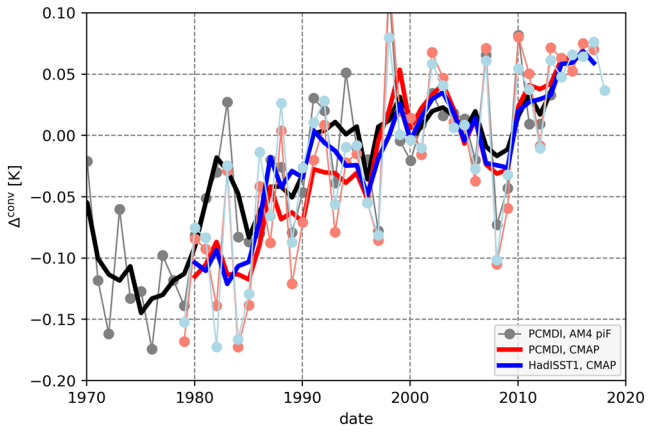

Figure 6. Evolution of annual means of Δ^{conv} in GFDL AM4 AMIP-piForcing simulations (black, mean over five ensembles) with SST from PCMDI/AMIPII, and observational estimates using CMAP rainfall with PCMDI/AMIPII (red) and HadISST1 (blue) SSTs. Data as in Figure 4; but for annual means (dots) and smoothed with 3-years running mean (lighter colors). Using GPCP rainfall instead of CMAP rainfall yields very similar results (Appendix, Figure A1).

in future work. The main result of interest here, however, is robust. For the 1980s and 1990s and considering the statistical 1-sigma uncertainty, the smallest trend in Δ^{conv} based on observed SST as obtained by the AMIP-piForcing simulations overlaps with trends in Δ^{conv} from coupled atmosphere-ocean GCMs. However, the statistical best estimate of the observed trend (including the AMIP-piForcing simulations) substantially exceeds the 95-percentile of the Δ^{conv} trends in the coupled GCM simulations. Thus, coupled atmosphere-ocean GCMs rarely show a trend in Δ^{conv} (or $SST^{\#}$) as large as observational SST reconstructions indicate for the 1980s and 1990s.

3. Discussion

The nonlinear relation between local surface temperature and the state of the overlying atmospheric column evident in the climatic base state (due to influence from nonlocal processes) implies that the writing of the state of the climate system as function of global average temperature (as done in the traditional definitions of climate sensitivity) is valid only if the statistics of the nonlinearity in the base state are stationary. The "pattern effect" noted in AMIP simulations violates this condition. Our results show that adding one more moment describing the distribution of surface conditions, $SST^{\#}$ or Δ^{conv}, is sufficient to explain the (low-pass filtered) evolution of the SWCRE in AMIP-piForcing simulations.

Our analysis has also highlighted inconsistencies in the observational record arising from differences in SST reconstructions, and to a lesser degree from differences in observational rainfall reconstructions. However, even the most conservative observational estimate of the trend in Δ^{conv} in the 1980s and 1990s is exceedingly rare in coupled atmosphere-ocean GCM simulations. Conceivable explanations include: (i) uncertainties in the observational record lead to artifacts in the SST record, and the large trend in $SST^{\#}$ and Δ^{conv} since the 1970s in the observational SST reconstructions is biased high; (ii) by coincidence the satellite era covers a very rare event of internal variability; (iii) coupled atmosphere-ocean GCM simulations miss a crucial process in the climate system. Option (iii) would constitute a major issue, but requires falsification of options (i) and (ii). We thus focus on options (i) and (ii).

Regarding option (i), we note that the magnitude of the trends in Δ^{conv} and $SST^{\#}$ is small (order 0.05 K/decade). For reference, trends in the equatorial Pacific SST gradient (discussed below) are about an order of magnitude larger. Thus, errors in the trends of Δ^{conv} and $SST^{\#}$ in the observational record may be possible even if the large-scale spatial patterns of SST trends are, as argued by Olonscheck et al. (2020) for the ERSSTv2, COBE2 and HadISST2 SST reconstructions, broadly consistent with the range covered by internal variability of coupled atmosphere-ocean GCMs. The verification of trends in Δ^{conv} from observations independent of SSTs is difficult. Trends in Δ^{conv} project on the amplification ratio of tropical upper tropospheric temperature trend to surface temperature trends (Flannaghan et al., 2014; Po-Chedley & Fu, 2012), but uncertainties in radiosonde trends are large (Mitchell et al., 2013) and the deep vertical kernel of the Microwave Sounding Unit measurements does not give enough signal to detect differences in the trend of Δ^{conv} (Po-Chedley et al., 2020). Similarly, lack of stable SWCRE measurements prior to the

Table 1
Linear Trends in Tropical Mean SST and SST# Over the Period (1900–2014), Their Ratio (in Percent), and the Difference ΔSST# Averaged Over (2000–2014) Minus the Average of (1900–1979)

SST reconstruction	d $\overline{\text{SST}}$ / dt (K/dec)	dSST#/dt (K/dec)	Ratio (%)	ΔSST# (K)
PCMDI/AMIPII	0.049	0.010	20.28	0.126
ERSSTv5	0.071	0.003	3.76	0.056
ERSSTv4	0.071	0.000	0.26	0.035
COBE	0.055	0.001	1.53	0.037
COBE2	0.059	0.001	1.46	0.038
HadISST1	0.047	0.004	7.67	0.057

Data as shown in Figure 3.

start of the CERES mission in March 2000 preclude direct observational confirmation of the impact on SWCRE. Also, variations in aerosol forcing (mainly from volcanoes) renders detection of the "pattern effect" in AMIP simulations with all forcings (as opposed to the AMIP piForcing simulations) difficult. These difficulties would also be present in the observational record. It is unfortunate that much of the CERES record to date coincides with the "hiatus" period where the SST reconstructions not only show little trend in $\overline{\text{SST}}$, but also in Δ^{conv} and SST#. While the CERES/EBAF record clearly shows that SST# contributes strongly to interannual variability (Ceppi & Gregory, 2017; Fueglistaler, 2019), it is too early to robustly detect whether SST# resumes the strong trend seen in the 1980s and 1990s, and whether the CERES/EBAF data shows a corresponding trend in SWCRE.

We have focused on the satellite era because SST observations are sparse in the presatellite period, and we hypothesize that in addition to known difficulties in homogenizing the ship-borne measurements, the methods employed for spatio-temporal extrapolation may induce spurious drifts and trends in SST#. These caveats notwithstanding, the presatellite period deserves attention because it provides context for the results obtained for the satellite period.

The observational SST reconstructions before the satellite era show oscillations in SST# of similar magnitude as the trend in the satellite era (Figure 3b). The satellite period stands out because the change is over 40 years, whereas in the presatellite period the trends over 40-year periods are much smaller, with one exception. The NOAA ERSST show a negative trend in SST# (which would imply an amplified positive SWCRE feedback) persisting from the 1870s to the 1930s that is not seen in any of the other SST reconstructions.

The PCMDI/AMIPII SSTs recommended for CMIP6 AMIP experiments stand out as having the largest increase in SST# (Table 1): over the period 1900 to 2014, the linear trend in SST# as well as the ratio to the trend in $\overline{\text{SST}}$, and the difference between the mean over the period 2000–2014 minus the mean over the period 1900–1978, are about twice that of HadISST1, and more relative to the other SSTs. Correspondingly, we expect that the "pattern effect" of a negative SWCRE feedback on long (100-years) timescale would be smaller in AMIP simulations forced with SSTs other than PCMDI/AMIPII. Thus, while the trends in SST# and Δ^{conv} are fairly robust across different SST reconstructions for the satellite period, the trends over the historical period (going back to the late 1800s) are not.

Lewis and Mauritsen (2021) indeed report that in AMIP-style GCM simulations and feedback calculations using a Greens function approach, the PCMDI/AMIPII reconstruction stands out compared to HadISST1 and other SST reconstructions (Had4_krig_v2, HadSST4krig_v2, COBE2) as being the only that has a large "pattern effect" over the period 1871 to 2010, consistent with the results shown in Table 1 (for direct comparison with Lewis & Mauritsen, 2021; Table C1 shows the results for their period 1871–2010). They also find ERSSTv5 at odds with the other SST reconstructions, though in this case it may be that the trends in the extratropics add an additional layer of complications. Over the full period 1871 to present, the ERSSTv4 and ERSSTv5 SSTs are the only ones where the convective regions warm less than the tropical average (see Figure 3b and Table C1; and Table 2 of Lewis & Mauritsen, 2021). However, in both the ERSSTv5 and PCMDI/AMIPII the tropical warm pool warms at the same rate as the average between 50°S and 50°N, but warms less in HadISST1 (and Had4_krig_v2, HadSST4krig_v2, COBE2). These differences have corresponding impacts on feedback estimates (see Lewis & Mauritsen, 2021, and their Table 2) and require attention in addition to the evolution of tropical SSTs discussed here.

Regarding option (ii), we note that the coupled atmosphere-ocean GCMs show a clear tendency to have a trend in Δ^{conv} that is proportional to the trend in $\overline{\text{SST}}$ (Figure 5). Internal variability leads to substantial scatter in the ratio of trends in Δ^{conv} and $\overline{\text{SST}}$, and a handful of segments of 36-years or 21-years length yield trends in Δ^{conv} and $\overline{\text{SST}}$ comparable to that in the observations over the satellite period. Internal variability thus cannot be entirely ruled out.

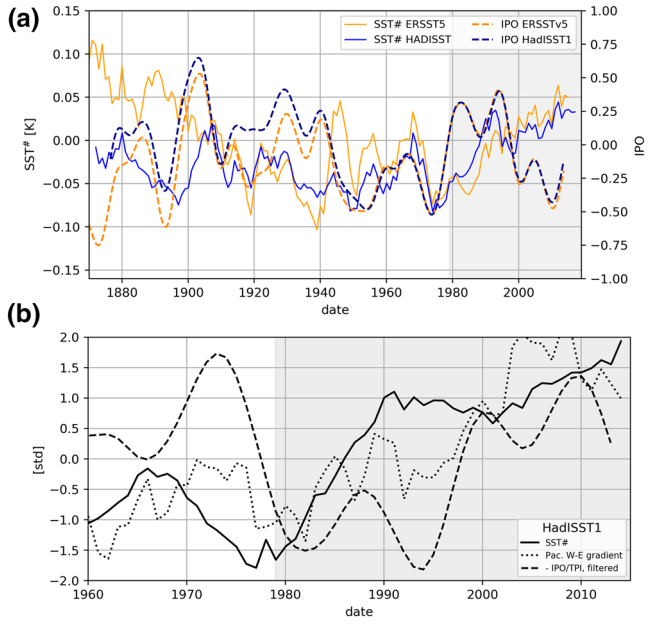

Figure 7. (a) Evolution of annual means of SST$^{\#}$ in HadISST1 and ERSSTv5 (as in Figure 3b, smoothed with 5-years running mean), and the filtered Interdecadal Pacific Oscillation (IPO) tripole index (Henley et al., 2015) determined from HadISST1 and ERSSTv5. (b) Evolution of SST$^{\#}$, filtered IPO index, and equatorial Pacific SST gradient (defined as the difference of SSTs in the domain (110 E–180 E, 5 S–5 N) minus the domain (180 E–280 E, 5 S–5 N)) since 1960 for HadISST1; in units of standard-deviations over the period shown. Note that in the panel (b) the sign of the IPO is inverted to allow better comparison; SST$^{\#}$ and SST gradient are smoothed with 11-years running means. Gray shading highlights the satellite period from 1979 onwards.

The question of internal variability is related to the question of the role of ocean heat uptake variations, and the cause of the hiatus in global warming. The abrupt change in the warming trend around the year 2000 is thought to be a consequence of a change in the oceanic heat uptake rate primarily in the Pacific basin (England et al., 2016; Kosaka & Xie, 2013; Meehl et al., 2013; Po-Chedley et al., 2020) with an ENSO-like geographical pattern of SST anomalies. The Interdecadal Pacific Oscillation (IPO) has been proposed to reflect these changes (Meehl et al., 2013), and the onset of the warming hiatus around the year 2000 follows a rapid change in the late 1990s from a positive to a negative phase in the IPO tripole index as defined by Henley et al. (2015). The equatorial Pacific East-West SST gradient plays a central role in this argument, with a steeper gradient implying a larger oceanic heat uptake rate. One may plausibly hypothesize that variations in the equatorial Pacific gradient and the IPO should project on SST$^{\#}$. The question whether the trend in the equatorial Pacific East-West SST gradient seen in the observational SST reconstructions over recent decades is consistent with results from coupled atmosphere-ocean GCMs has in itself received much attention (e.g. Coats & Karnauskas, 2017; Olonscheck et al., 2020; Watanabe et al., 2021). The recent analysis by Watanabe et al. (2021) suggests that the steepening of the gradient is consistent with the model simulations when considering internal variability.

Figure 7(a) shows the evolution of the IPO tripole index as provided by NOAA since the late 1800s to the present calculated from HadISST1 and ERSSTv5. A drift between the two is noted in the 1930s/1940s, but generally they are highly correlated, in particular since the 1940s. There is no clear relation, however, between the IPO index and SST$^{\#}$ over the full period since the 1870s. For visual clarity of the evolution in recent decades, Figure 7(b) shows the timeseries for HadISST1 since 1960, and also shows the equatorial Pacific West-East SST gradient. Note that the definition of the gradient used here (West minus East) conforms with the sign of SST$^{\#}$. Similarly, for better visual comparison with SST$^{\#}$, Figure 7(b) shows the IPO with flipped sign. The figure shows that over the satellite period the three indexes all have a minimum (maximum for IPO) in the late 1970s and a maximum (minimum for IPO) toward the end of the period, but differences in phase in-between. In the 1980s and early 1990s when SST$^{\#}$ shows a strong positive trend and the SWCRE feedback is strongly negative (Silvers et al., 2018; Zhou et al., 2016, and Figure 1), the IPO index is positive and the equatorial Pacific SST gradient is small (indicative of reduced oceanic heat uptake and implied enhanced global warming). Conversely, the large shift in the IPO index in the late 1990s leading to the subsequent warming hiatus is associated with no change in Δ^{conv}. The presatellite period does not help to clarify the situation as there is little persistent systematic relation between the IPO index and SST$^{\#}$, and there are substantial differences between the two SST reconstructions in the IPO index (compare dashed lines in Figure 7a) and in particular in SST$^{\#}$ (compare solid lines in Figure 7a).

It seems rather ironic that exactly the best-observed satellite period shows rare behavior compared to coupled atmosphere-ocean GCM simulations: an extended hiatus in global warming and a large trend in Δ^{conv} (and SST$^{\#}$) in the 1980s and 1990s. These signals are present in all SST reconstructions considered here (PCMDI/AMIPII, HadISST1, COBE, COBE2, ERSSTv4, and ERSSTv5; see Figure 3), but the PCMDI/AMIPII reconstruction stands out as having a larger increase in SST$^{\#}$ over the satellite era relative to the presatellite era.

The substantial differences between SST reconstructions preclude definitive conclusions regarding the processes controlling Δ^{conv}, and whether there has been a strong trend therein over the satellite period, leading to a pronounced negative SWCRE feedback. This work highlights how critical continuous, high quality satellite data is for estimating present-day climate sensitivity, and for validating and improving global climate models. Based on the currently available observational data, one may conclude that the trajectory of the state of the climate system over the observational period is peculiar.

Appendix A: Sensitivity of Δ to rainfall data

Figure A1a shows that: (i) the AM4 AMIP-piForcing simulations show some differences among ensembles; (ii) the CMIP6 AMIP simulations show some differences between models for one ensemble that is similar to the differences seen among the AM4 AMIP-piForcing ensembles; (iii) the results for AMIP-piForcing simulations and CMIP6 AMIP simulations are very similar despite the lack of atmospheric forcing in the AMIP-piForcing simulations; and (iv) the AMIP-piForcing and AMIP simulations are more similar to each other than to the observational estimates.

Figure A1b focuses on the differences between the model simulations using observed SSTs and the estimates using observed rainfall. Differences are most prominent in the early/mid 1980s and early/mid 1990s.

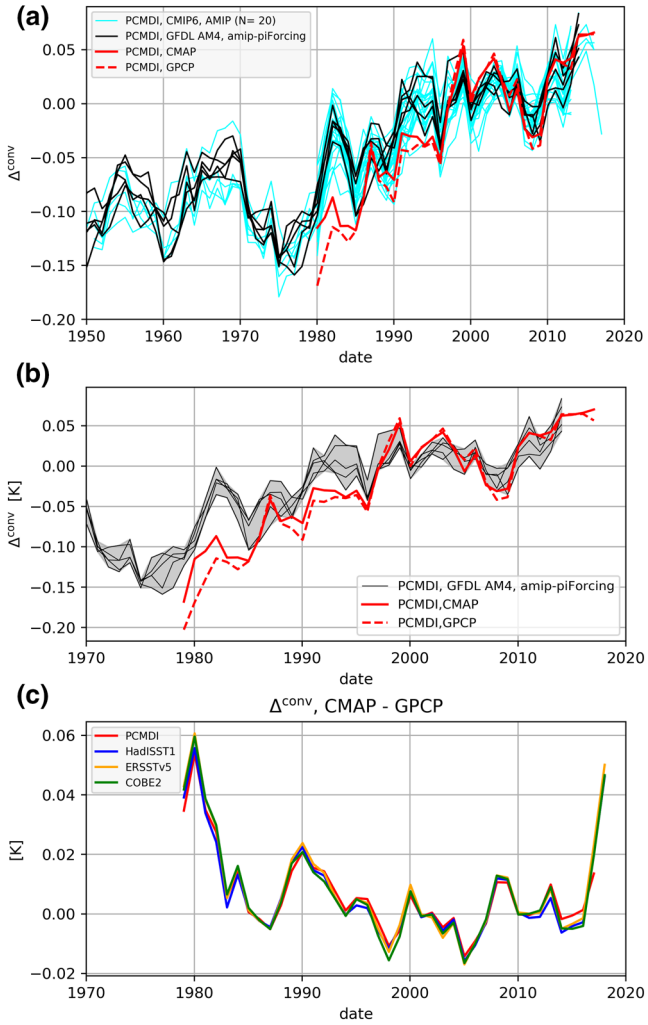

Figure A1. (a) Δ^{conv} from GFDL AM4 AMIP-piForcing simulation (5 ensemble members), CMIP6 AMIP simulations (one ensemble from 20 models), and the estimates using rainfall from GPCP and CMAP. All calculations use PCMDI/AMIPII SSTs. Annual mean data smoothed with a 3-years running mean for visual clarity. (b) As in (a), but without CMIP6 AMIP results; range of AM4 AMIP-piForcing simulations indicated with gray shading for visual clarity regarding the agreement with the estimates using observed rainfall. (c) The difference in Δ^{conv} in the observational estimates between GPCP and CMAP using PCMDI/AMIPII SSTs (i.e., the difference between the red solid and dashed lines in panels a/b), and using different SST reconstructions (HadISST1, ERSST5, and COBE2).

Figure A1c shows that the differences in the observational estimates using GPCP and CMAP rainfall are not sensitive to SST data used (differences post 2010 noted). The difference in the observational estimate due to differences between GPCP and CMAP rainfall is largest in the first few years since 1979, which contributes to the difference in the trends in Δ^{conv} since 1979.

Appendix B: Statistics of trends 1979–2000, and 21-years segments

Figure B1 is similar to Figure 5, but given that the trend in Δ^{conv} is most prominent in the 1980s and 1990s, the figure shows the trends in $\overline{SST}$ and Δ^{conv} evaluated over 21-year periods rather than 36-year periods. The figure shows that (i) the trends in the observational estimates and the AM4 AMIP-piForcing simulations for 1979–2000 are larger than for 1979–2014 (as expected); (ii) the statistical uncertainty increases (as expected for the shorter time period); (iii) correspondingly coupled atmosphere-ocean GCM simulations have a wider spread in amplification ratio than over the longer 36-year period; (iv) the observational and AMIP-piForcing estimates are still extremely unusual compared to the coupled atmosphere-ocean GCM results.

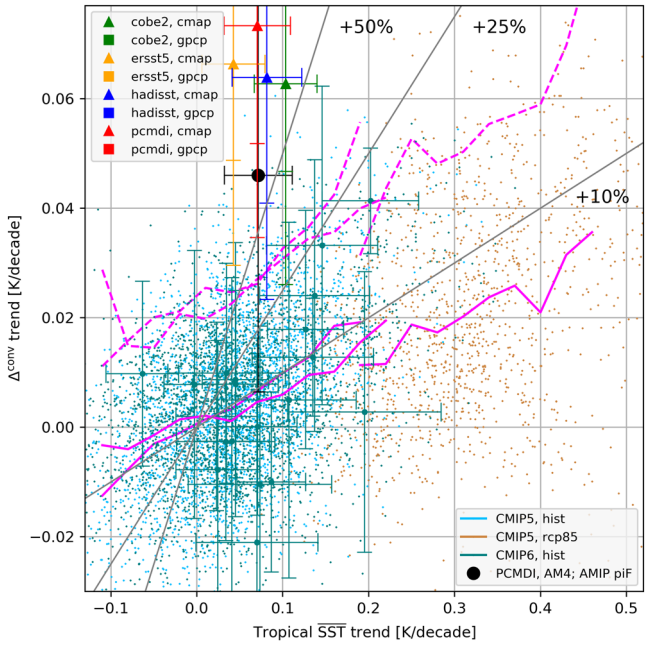

Figure B1. Scatter plot of trends in tropical average SST ($\overline{SST}$, *x*-axis) against trends in Δ^{conv} (*y*-axis), evaluated over 21-year periods (i.e., as Figure 5, but with 21-year periods and 1-sigma uncertainty shown for the CMIP6 trends over the period 1979–2000). Colors and symbols as labeled; one ensemble per model over all (including overlapping) 21-year periods. The average and 95-percentile Δ^{conv} trend as function of trend in tropical average SST for each experiment (CMIP5 historical, CMIP6 historical and CMIP5 RCP8.5 scenario) are shown in magenta (solid and dashed, respectively) for tropical average SST trends with more than 50 realizations. The observational estimates (as labeled in legend) and the CMIP5 and CMIP6 model trends of the specific period 1979–2000 are shown with their 1-sigma statistical error. Note that Δ^{conv} trends calculated for the observations with GPCP precipitation are larger than the maximum of the y-axis. Gray lines indicate where the trend in Δ^{conv} is 10%, 25%, and 50% of the trend $\overline{SST}$ (i.e., SST trends in regions of deep convection are larger by that percentage than the tropical average SST trend).

Appendix C: Trends of mean SST and SST# over the period 1871–2010

Table C1 is similar to Table 1, but the trends are calculated for the period (1871–2010) for direct comparison with the results presented by (Lewis & Mauritsen, 2021) for that period.

Table C1
Linear Trends in Tropical Mean SST and SST# Over the Period [1871-2010], and Their Ratio (in Percent). Data as Shown in Figure 3; Period For Trends as in Lewis and Mauritsen (2021)

SST reconstruction	$d\overline{SST}/dt$ (K/dec)	$dSST^{\#}/dt$ (K/dec)	Ratio (%)
PCMDI/AMIPII	0.038	0.006	14.91
ERSSTv5	0.042	−0.005	−12.31
ERSSTv4	0.043	−0.006	−14.60
COBE	0.049	−0.001	−1.91
COBE2	0.044	−0.002	−4.73
HadISST1	0.036	0.001	3.95

Appendix D: List of CMIP5 and CMIP6 models

Simulations (one ensemble per model) of the following models have been used:

CMIP5 historical

CESM1-CAM5, CMCC-CESM, CMCC-CM, CMCC-CMS, CNRM-CM5, CNRM-CM5-2, CSIRO-Mk3-6-0, CanESM2, GFDL-CM2p1, GFDL-CM3, GFDL-ESM2G, GFDL-ESM2M, GISS-E2-H, GISS-E2-H-CC, GISS-E2-R, GISS-E2-R-CC, HadGEM2-AO, inmcm4, IPSL-CM5A-MR, IPSL-CM5B-LR, MIROC-ESM, MIROC5, MPI-ESM-MR, MPI-ESM-P, MRI-CGCM3, NorESM1-M, NorESM1-ME.

CMIP5 RCP8.5

CCSM4, CESM1-CAM5, CMCC-CESM, CMCC-CM, CMCC-CMS, CNRM-CM5, CSIRO-Mk3-6-0, CanESM2, GFDL-CM3, GFDL-ESM2G, GFDL-ESM2M, inmcm4, IPSL-CM5B-LR, MIROC-ESM, MIROC5, MPI-ESM-MR, MRI-CGCM3, NorESM1-M.

CMIP6 historical

BCC-CSM2-MR, BCC-ESM1, CAMS-CSM1-0, CESM2, CESM2-WACCM, CanESM5, EC-Earth3, EC-Earth3-Veg, FGOALS-g3, GFDL-CM4, GFDL-ESM4, GISS-E2-1-G, GISS-E2-1-H, IPSL-CM6A-LR, MIROC6, MPI-ESM1-2-HR, MRI-ESM2-0, NESM3, NorCPM1, SAM0-UNICON.

Data Availability Statement

The authors thank the GFDL Atmospheric Working Group (AWG) for developing AM4, and for providing the AM4 AMIP-piForcing simulations. The authors thank the following agencies for providing free access to their data: The UK Met Office and the Hadley Center for providing the HadISST data, downloaded online at https://www.metoffice.gov.uk/hadobs/hadisst; GPCP data provided by the NASA/Goddard Space Flight Center's Mesoscale Atmospheric Processes Laboratory, which develops and computes the 1DD as a contribution to the GEWEX Global Precipitation Climatology Project. Data set accessed online at https://www.ncei.noaa.gov/data/global-precipitation-climatology-project-gpcp-monthly/access/.

CMAP Precipitation data provided by the NOAA/OAR/ESRL PSL, Boulder, Colorado, USA, from their Web site at https://psl.noaa.gov; data downloaded from https://psl.noaa.gov/data/gridded/data.cmap.html. NOAA_ERSST_V4 data provided by the NOAA/OAR/ESRL PSL, Boulder, CO, USA, from their Web site at https://psl.noaa.gov; data downloaded from https://www1.ncdc.noaa.gov/pub/data/cmb/ersst/v4/netcdf/. NOAA_ERSST_V5 data provided by the NOAA/OAR/ESRL PSL, Boulder, CO, USA, from their Web site at https://psl.noaa.gov; data downloaded from https://www1.ncdc.noaa.gov/pub/data/cmb/ersst/v5/netcdf/. COBE-SST and COBE-SST2 data provided by the NOAA/OAR/ESRL PSL, Boulder, CO, USA, from their Web site at https://psl.noaa.gov; data downloaded from https://psl.noaa.gov/data/gridded/data.cobe.html and https://psl.noaa.gov/data/gridded/data.cobe2.html. We acknowledge the World Climate Research Program, which, through its Working Group on Coupled Modeling, coordinated and promoted CMIP5 and CMIP6. We thank the climate modeling groups for producing and making available their model output, the Earth System Grid Federation (ESGF) for archiving the data and providing access, and the multiple funding agencies who support CMIP and ESGF. All CMIP data are available from the ESGF at https://esgf-node.llnl.gov/projects/esgf-llnl/.

Acknowledgments
S. Fueglistaler acknowledges support from the National Science Fund Awards PIRE-1743753, AGS-1660538, and AGS-1733818. L. Silvers acknowledges support from the Cooperative Institute for Climate Sciences, Princeton. L. Silvers contributions were prepared under award NA18OAR4320123 from the National Oceanic and Atmospheric Administration, U.S. Department of Commerce. L. Silvers also acknowledges recent partial support through Stony Brook University from award DE-SC0019459. The statements, findings, conclusions, and recommendations are those of the authors and do not necessarily reflect the views of the National Oceanic and Atmospheric Administration, or the U.S. Department of Commerce.

References

Adler, R., Huffman, G., Chang, A., Ferraro, R., Xie, P.-P., Janowiak, J., et al. (2003). The version-2 global precipitation climatology project (GPCP) monthly precipitation analysis (1979–present). *Journal of Hydrometeorology*, *4*, 1147–1167. https://doi.org/10.1175/1525-7541(2003)004%3C1147:TVGPCP%3E2.0.CO;2

Allan, R., Soden, B., John, V., Ingram, W., & Good, P. (2010). Current changes in tropical precipitation. *Environmental Research Letters*, *5*, 025205. https://doi.org/10.1088/1748-9326/5/2/025205

Anderson, T. L., Charlson, R. J., Schwartz, S. E., Knutti, R., Boucher, O., Rodhe, H., & Heintzenberg, J. (2003). Climate forcing by aerosols: A hazy picture. *Science*, *300*, 1103–1104. https://doi.org/10.1126/science.1084777

Andrews, T., Gregory, J., Paynter, D., Silvers, L., Zhou, C., Mauritsen, T., et al. (2018). Accounting for changing temperature patterns increases historical estimates of climate sensitivity. *Geophysical Research Letters*, *45*, 8490–8499. https://doi.org/10.1029/2018GL078887

Andrews, T., & Webb, M. J. (2018). The dependence of global cloud and lapse rate feedbacks on the spatial structure of tropical pacific warming. *Journal of Climate*, *31*(2), 641–654. https://doi.org/10.1175/JCLI-D-17-0087.1

Bony, S., & Dufresne, J.-L. (2005). Marine boundary layer clouds at the heart of tropical cloud feedback uncertainties in climate models. *Geophysical Research Letters*, *32*, L20806. https://doi.org/10.1029/2005GL023851

Bretherton, C. (2015). Insights into low-latitude cloud feedbacks from high-resolution models. *Philosophical Transactions of the Royal Society A*, *373*, 20140415. https://doi.org/10.1098/rsta.2014.0415

Ceppi, P., & Gregory, J. (2017). Relationship of tropospheric stability to climate sensitivity and earth's observed radiation budget. *Proceedings of the National Academy of Sciences*, *114*, 13126–13131. https://doi.org/10.1073/pnas.1714308114

Coats, S., & Karnauskas, K. (2017). Are simulated and observed twentieth century tropical pacific sea surface temperature trends significant relative to internal variability? *Geophysical Research Letters*, *44*, 9928–9937. https://doi.org/10.1002/2017GL074622

Dong, Y., Proistosescu, C., Armour, K., & Battisti, D. (2019). Attributing historical and future evolution of radiative feedbacks to regional warming patterns using a green's function approach: The pre-eminence of the western pacific. *Journal of Climate*. *32*(17), 5471–5491. https://doi.org/10.1175/JCLI-D-18-0843.1

England, M., McGregor, S., Spence, P., Meehl, G., Timmermann, A., Cai, W., et al. (2016). Recent intensification of wind-driven circulation in the pacific and the ongoing warming hiatus. *Nature Climate Change*, *4*, 222–227. https://doi.org/10.1038/NCLIMATE2106

Flannaghan, T. J., Fueglistaler, S., Held, I. M., Po-Chedley, S., Wyman, B., & Zhao, M. (2014). Tropical temperature trends in atmospheric general circulation model simulations and the impact of uncertainties in observed SSTs. *Journal of Geophysical Research*, *119*(27), 13327–13337. https://doi.org/10.1002/2014JD022365

Fueglistaler, S. (2019). Observational evidence for two modes of coupling between sea surface temperatures, tropospheric temperature profile, and shortwave cloud radiative effect in the tropics. *Geophysical Research Letters*, *46*, 9890–9898. https://doi.org/10.1029/2019GL083990

Fueglistaler, S., Radley, C., & Held, I. M. (2015). The distribution of precipitation and the spread in tropical upper tropospheric temperature trends. *Geophysical Research Letters*, *42*(14), 6000–6007. https://doi.org/10.1002/2015GL064966

Gregory, J. M., & Andrews, T. (2016). Variation in climate sensitivity and feedback parametersduring the historical period. *Geophysical Research Letters*, *43*, 3911–3920. https://doi.org/10.1002/2016GL068406

Gregory, J. M., Andrews, T., Ceppi, P., Mauritsen, T., & Webb, M. (2019). How accurately can the climate sensitivity to co2 be estimated from historical climate change? *Climate Dynamics*, *54*, 129–157. https://doi.org/10.1007/s00382-019-04991-y

Henley, B., Gergis, J., Karoly, D., Power, S., Kennedy, J., & Folland, C. (2015). A tripole index for the interdecadal pacific oscillation. *Climate Dynamics*, *45*(11–12), 3077–3090. https://doi.org/10.1007/s00382-015-2525-1

Horel, J. D., & Wallace, J. M. (1981). Planetary-scale atmospheric phenomena associated with the southern oscillation. *Monthly Weather Review*, *109*, 813–829. https://doi.org/10.1175/1520-0493(1981)109%3C0813:PSAPAW%3E2.0.CO;2

Hoskins, B. J., & Karoly, D. J. (1981). The steady linear response of a spherical atmosphere to thermal and orographic forcing. *Journal of the Atmospheric Sciences*, *38*(6), 1179–1196. https://doi.org/10.1175/1520-0469(1981)038<1179:TSLROA>2.0.CO;2

Huang, B., Thorne, P. W., Banzon, V. F., Boyer, T., Chepurin, G., Lawrimore, J. H., et al. (2017). NOAA extended reconstructed sea surface temperature (ERSST) version 5. *Journal of Climate*, *30*(12), 8179–8205. https://doi.org/10.7289/V5T72FNM

Huffman, G. J., Adler, R. F., Morrissey, M. M., Bolvin, D. T., Curtis, S., Joyce, R., Susskind, et al. (2001). Global precipitation at one-degree daily resolution from multisatellite observations. *Journal of Hydrometeorology*, *2*(1), 36–50. https://doi.org/10.1175/1525-7541(2001)002%3C0036:GPAODD%3E2.0.CO;2

Hurrell, J. W., Hack, J. J., Shea, D., Caron, J. M., & Rosinski, J. (2008). A new sea surface temperature and sea ice boundary dataset for the community atmosphere model. *Journal of Climate*, *21*(19), 5145–5153. https://doi.org/10.1175/2008JCLI2292.1

IPCC. (2013). Climate Change 2013: The Physical Science Basis. In T. F. Stocker, D. Qin, G.-K. Plattner, M. Tignor, S. K. Allen, J. Boschung, et al. (Eds.), *Contribution of Working Group I to the Fifth Assessment Report of the Intergovernmental Panel on Climate Change*, (p. 1535). Cambridge, UK; New York, USA: Cambridge University Press.

IPCC. (2018). Summary for Policymakers. In V. Masson-Delmotte, P. Zhai, H.-O. Pörtner, D. Roberts, J. Skea, P. R. Shukla, et al. (Eds.), *Global Warming of 1.5°C. An IPCC Special Report on the impacts of global warming of 1.5°C above pre-industrial levels and related global greenhouse gas emission pathways, in the context of strengthening the global response to the threat of climate change, sustainable development, and efforts to eradicate poverty* (p. 32). Geneva, Switzerland: World Meteorological Organization.

Jimenez-de-la Cuesta, D., & Mauritsen, T. (2019). Emergent constraints on Earth's transient and equilibrium response to doubled CO_2 from post-1970s global warming. *Nature Geoscience*, *12*, 902–905. https://doi.org/10.1038/s41561-019-0463-y

Kiehl, J. (2007). Twentieth century climate model response and climate sensitivity. *Geophysical Research Letters*, *34*, L22710. https://doi.org/10.1029/2007GL031383

Klein, S. A., & Hartmann, D. L. (1993). The seasonal cycle of low stratiform clouds. *Journal of Climate*, *6*(8), 1587–1606. https://doi.org/10.1175/1520-0442(1993)006<1587:TSCOLS>2.0.CO;2

Kosaka, Y., & Xie, S.-P. (2013). Recent global-warming hiatus tied to equatorial pacific surface cooling. *Nature*, *501*, 403–407. https://doi.org/10.1038/nature12534

Lewis, N., & Mauritsen, T. (2021). Negligible unforced historical pattern effect on climate feedback strength found in HadISST-based AMIP simulations. *Journal of Climate*, *34*, 39–55. https://doi.org/10.1175/JCLI-D-19-0941.1

Loeb, N., Wang, H., Su, W., Nguyen, C., Corbrett, J., Liang, L., et al. (2018). Clouds and the earth's radiant energy system (CERES) energy balanced and filled (EBAF) top-of-atmosphere (TOA) edition-4.0 data product. *Journal of the Atmospheric Sciences*, *31*, 895–918. https://doi.org/10.1175/JCLI-D-17-0208.1

Meehl, G., Arblaster, J. M., Fasullo, J. Y., Hu, A., & Trenberth, K. E. (2011). Model-based evidence of deep-ocean heat uptake during surface-temperature hiatus periods. *Nature Climate Change*, *1*, 360–364. https://doi.org/10.1038/NCLIMATE1229

Meehl, G., Hu, A., Arblaster, J. M., Fasullo, J., & Trenberth, K. E. (2013). Externally forced and internally generated decadal climate variability associated with the interdecadal pacific oscillation. *Journal of Climate*, *26*, 7298–7310. https://doi.org/10.1175/JCLI-D-12-00548.1

Miller, R. (1997). Tropical thermostats and low cloud cover. *Journal of Climate*, *10*, 409–440. https://doi.org/10.1175/1520-0442(1997)010<0409:TTALCC>2.0

Mitchell, D. M., Thorne, P. W., Stott, P. A., & Gray, L. (2013). Revisiting the controversial issue of tropical tropospheric temperature trends. *Geophysical Research Letters*, *40*, 2801–2806. https://doi.org/10.1002/grl.50465

Olonscheck, D., Rugenstein, M., & Marotzke, J. (2020). Broad consistency between observed and simulated trends in sea surface temperature patterns. *Geophysical Research Letters*, *47*, e2019GL086773. https://doi.org/10.1029/2019GL086773

O'Reilly, C. H., Woollings, T., Zanna, L., & Weisheimer, A. (2019). An interdecadal shift of the extratropical teleconnection from the tropical pacific during boreal summer. *Geophysical Research Letters*, *46*, 13379–13388. https://doi.org/10.1029/2019GL084079

Po-Chedley, S., Armour, K., Bitz, C., Zelinka, M., & Santer, B. (2018). Sources of intermodel spread in the lapse rate and water vapor feedbacks. *Journal of Climate*, *31*, 3187–3206. https://doi.org/10.1175/JCLI-D-17-0674.1

Po-Chedley, S., & Fu, Q. (2012). Discrepancies in tropical upper tropospheric warming between atmospheric circulation models and satellites. *Environmental Research Letters*, *7*, 044018. https://doi.org/10.1088/1748-9326/7/4/044018

Po-Chedley, S., Santer, B. D., Fueglistaler, S., Zelinka, M., Cameron-Smith, P., Painter, J., & Fu, Q. (2020). Natural variability contributes to model-satellite differences in tropical tropospheric warming. *Proceedings of the National Academy of Sciences*. https://www.osti.gov/servlets/purl/1698285

Rayner, N. A., Parker, D. E., Horton, E. B., Folland, C. K., Alexander, L. V., Rowell, D. P., et al. (2003). Global analyses of sea surface temperature, sea ice, and night marine air temperature since the late nineteenth century. *Journal of Geophysical Research*, *108*(D14), 4407. https://doi.org/10.1029/2002JD002670

Santer, B., Solomon, S., Pallotta, G., Mears, C., Po-Chedley, S., Fu, Q., et al. (2017). Comparing tropospheric warming in climate models and satellite data. *Journal of Climate*, *30*, 373–392. https://doi.org/10.1175/JCLI-D-16-0333.1

Sherwood, S. C., Webb, M. J., Annan, J. D., Armour, K. C., Forster, P. M., Hargreaves, J. C., & et al. (2020). An assessment of earth's climate sensitivity using multiple lines of evidence. *Reviews of Geophysics*, *58*, e2019RG000678. https://doi.org/10.1029/2019RG000678

Silvers, L., Paynter, D., & Zhao, M. (2018). The diversity of cloud responses to twentieth century sea surface temperatures. *Geophysical Research Letters*, *45*(1), 391–400. https://doi.org/10.1002/2017GL075583

Smith, T., Sapiano, M., & Arkin, P. (2009). Modes of multi-decadal oceanic precipitation variations from a reconstruction and AR-4 model output for the 20th century. *Geophysical Research Letters*, *36*, L14708. https://doi.org/10.1029/2009GL039234

Stevens, B., Sherwood, S., Bony, S., & Webb, M. (2016). Prospects for narrowing bounds on earth's equilibrium climate sensitivity. *Earth's Future*, *4*(11), 512–522. https://doi.org/10.1002/2016EF000376

Trenberth, K. E., Branstator, G. W., Karoly, D., Kumar, A., Lau, N., & Ropelewski, C. (1998). Progress during toga in understanding and modeling global teleconnections associated with tropical sea surface temperatures. *Journal of Geophysical Research*, *103*(C7) 14291–14324. https://doi.org/10.1029/97JC01444

Waliser, D. E., & Graham, N. E. (1993). Convective cloud systems and warm-pool sea surface temperatures: Coupled interactions and self-regulation. *Journal of Geophysical Research*, *98*(D7), 12881–12893. https://doi.org/10.1029/93JD00872

Watanabe, M., Dufresne, J.-L., Kosaka, Y., Mauritsen, T., & Tatebe, H. (2021). Enhanced warming constrained by past trends in equatorial pacific sea surface temperature gradient. *Nature Climate Change*, *11*, 33–37. https://doi.org/10.1038/s41558-020-00933-3

Wood, R. (2012). Stratocumulus clouds. *Monthly Weather Review*, *140*, 2373–2423. https://doi.org/10.1175/MWR-D-11-00121.1

Wood, R., & Bretherton, C. (2006). On the relationship between stratiform low cloud cover and lower-tropospheric stability. *Journal of Climate*, *19*, 6425–6432. https://doi.org/10.1175/JCLI3988.1

Xie, P., & Arkin, P. (1997). Global precipitation: A 17-year monthly analysis based on gauge observations, satellite estimates, and numerical model outputs. *Bulletin of the American Meteorological Society*, *78*, 2539–2558. https://doi.org/10.1175/1520-0477(1997)078<2539:GPAYMA>2.0

Zelinka, M. D., Myers, T. A., McCoy, D. T., Po Chedley, S., Caldwell, P. M., Ceppi, P., et al. (2020). Causes of higher climate sensitivity in CMIP-6 models. *Geophysical Research Letters*, *47*, e2019GL085782. https://doi.org/10.1029/2019GL085782

Zhang, C. (1993). Large-scale variability of atmospheric deep convection in relation to sea surface temperature in the tropics. *Journal of Climate*, *6*(10), 1898–1913. https://doi.org/10.1175/1520-0442(1993)006<1898:LSVOAD>2.0

Zhang, Y., & Fueglistaler, S. (2020). How tropical convection couples high moist static energy over land and ocean. *Geophysical Research Letters*, *47*(2), e2019GL086387. https://doi.org/10.1029/2019GL086387

Zhao, M., Golaz, J.-C., Held, I. M., Guo, H., Balaji, V., Benson, R., et al. (2018). The GFDL global atmosphere and land model AM 4.0/LM 4.0: 1. simulation characteristics with prescribed SSTS. *Journal of Advances in Modeling Earth Systems*, *10*, 691–734. https://doi.org/10.1002/2017MS001208

Zhao, M., Golaz, J.-C., Held, I. M., Guo, H., Balaji, V., Benson, R., et al. (2018). The GFDL global atmosphere and land model AM 4.0/LM 4.0: 2. model description, sensitivity studies, and tuning strategies. *Journal of Advances in Modeling Earth Systems*, *10*, 735–769. https://doi.org/10.1002/2017MS001209

Zhou, C., Zelinka, M., & Klein, S. (2016). Impact of decadal cloud variations on the earth's energy budget. *Nature Geoscience*, *9*, 871–874. https://doi.org/10.1038/ngeo2828